

Dynamical regimes of CCN activation in adiabatic air parcels

Manuel Santos Gutiérrez¹, Mickaël D. Chekroun¹, and Ilan Koren¹

¹Department of Earth and Planetary Sciences, Weizmann Institute of Science, Rehovot 76100, Israel

Correspondence: Manuel Santos Gutiérrez (manuel.santos-gutierrez@weizmann.ac.il)

Abstract. Ubiquitous, yet elusive to a complete understanding: Tiny, warm clouds with faint visual signatures play a critical role in Earth's energy balance. These "twilight clouds", as they are sometimes called, form under weak updraft conditions. Their constituent particles exist in a precarious state, teetering between hazy wisps and activated droplets. This delicate thermodynamic balance creates a limited reservoir of supersaturation, which activated droplets readily consume. Our research presents a novel approach, solving coupled equations for particle growth (Köhler's equation) and supersaturation change. This reveals previously unconsidered activation states for these clouds. Additionally, the analysis predicts conditions where particles can exhibit self-sustained oscillations between haze and activated droplet states.

1 Introduction

The coupling of cloud microphysics with climate dynamics is one of the most challenging problems in the atmospheric sciences. Far from being solved, the problem of cloud parameterization is responsible for the largest sources of uncertainty in global climate projections (Zelinka et al., 2020). The large spatial scale separation between general circulation and convective motions, the inherent complexity of cloud motion and the current computational power, demand a more accurate description of the nonlinear processes in the onset and development of clouds.

From all the cloud types, the warm and smallest ones are particularly difficult to parameterize in climate models despite being vastly abounding in Earth's atmosphere (Koren et al., 2007; Várnai and Marshak, 2009; Eytan et al., 2020). Specifically, "twilight clouds" are the most challenging to capture due to their poor optical signature. Regarding their microphysical structure, these small clouds are likely to re-

side near the transition from haze to activated cloud droplets, a domain of sizes difficult to resolve in current large-scale numerical models. Some of the latter clouds were shown to form in buoyant humidity pockets— often forming subLCL clouds (Hirsch et al., 2015, 2017; Altaratz et al., 2021)—, that oscillate between these two thermodynamic states due to the weak updraft in which they are embedded. The transition from haze to activated cloud droplets is described by Köhler's theory. This study aims to understand the dynamics of droplet's transitions relevant to twilight clouds.

While Köhler's theory (Köhler, 1936) explains how individual cloud condensation nuclei (CCN) activate into droplets based on critical humidity and radius, it treats single particles. For a real cloud with many CCNs in the same space, we need to consider how growing droplets affect the surrounding supersaturation (Korolev and Mazin, 2003), (Pinsky et al., 2013, Eq. 42). Cloud models typically couple droplet growth with supersaturation change after activation, e.g. (Khain et al., 2008; Khain and Pinsky, 2018). Köhler's theory assumes slow supersaturation depletion compared to droplet growth, which works well for vigorous clouds. In contrast, this study focuses on the fate of collections of monodisperse particles taken together in situations with weak updrafts, where supersaturation sources are limited and droplet sizes remain near critical values.

2 The supersaturation-radius-Köhler (SRK) equation

We consider a vertically moving adiabatic air parcel seeded with a monodisperse family of aerosols of the same size and chemistry. The small size of CCN provokes that their curvatures increase the equilibrium vapor pressure, so that humidity values above saturation are needed to activate a water droplet. The curvature effect is also counteracted by the CCN's chemical ability to retain water and their combination is the content of Köhler theory (Köhler, 1936; Pruppacher and Klett, 2010).

If S denotes liquid-water supersaturation and r the radius of a particle, the rate of change of r , with respect to time, is assumed to take the form:

$$\dot{r} = \frac{D}{r} \left(S - \frac{A}{r} + \frac{B}{r^3} \right), \quad (1)$$

where A/r , is Kelvin's curvature effect and, B/r^3 is Raoult's term and D is the temperature-dependent diffusional parameter; see Appendix A. The right-hand-side of Eq. (1) is a truncation of the Köhler curve which originally takes an exponential form, see e.g. Wallace and Hobbs (2006); Arabas and Shima (2017); Prabhakaran et al. (2020). For large values of r , saturation, $S > 0$ is enough to induce condensational growth, since $\dot{r} > 0$.

Analyzing the function $f(r) = Ar^{-1} - Br^{-3}$ reveals a single global maximum at $r_c = \sqrt{3B/A}$ and associated supersaturation $S_c = f(r_c) = Ar_c^{-1} - Br_c^{-3} = 2A/3r_c$. Such values are called the critical radius and supersaturation, respectively. Indeed, if $S > S_c$, it follows that equation (1) does not have an equilibrium and therefore, the particle radius $r(t)$ grows indefinitely, entering the activated state. If $0 < S < S_c$, two equilibria are allowed, of radii $r_h < r_c$ and $r_u > r_c$. The equilibrium r_h is stable and represents haze, i.e., humidified particles which do not grow with the available supersaturation. The equilibrium r_u is unstable. It reflects a threshold size beyond which a particle activates and becomes hygroscopic. An example of Köhler curve, $f(r)$, for salt is shown in Fig. 1. As supersaturation increases, the haze and unstable equilibrium collide, provoking model (1) to undergo a saddle-node bifurcation leading to the activation of a droplet (Arabas and Shima, 2017).

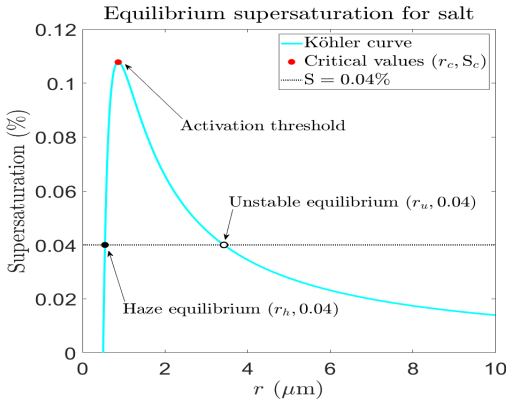


Figure 1. The cyan curve is the Köhler curve for the equilibrium supersaturation for a small salt aerosol. Here, we consider a salt particle of dry radius $0.065\mu\text{m}$. The dashed line indicates an example fixed supersaturation equation to 0.04% . The surface tension parameter is $A = 1.4 \cdot 10^{-3}\mu\text{m}$ and the chemistry coefficient, $B = 3.5 \cdot 10^{-4}\mu\text{m}^3$.

Köhler's critical values are often used as an activation threshold (red dot in Fig. 1). However, they assume a slowly

depleting humidity reservoir, limiting their applicability to describing the collective activation of many droplets. When supersaturation (S) becomes time-dependent, its sources and sinks become crucial. By taking the time derivative of S , we arrive at its evolution equation (Squires, 1952; Korolev and Mazin, 2003):

$$\frac{1}{1+S} \frac{dS}{dt} = \tau^{-1} - \beta \frac{dq}{dt}, \quad (2)$$

Here, β (defined in Appendix A) accounts for the latent heat released during condensation. The variable q represents the liquid-water mixing ratio, and τ^{-1} is the supersaturation timescale. This timescale is typically determined by the product of vertical velocity (w) and the adiabatic parameter (a_0), as detailed in Appendix A; see also (Pruppacher and Klett, 2010). In this specific case, $\tau^{-1} = a_0 w$ reflects the increase in supersaturation due to adiabatic cooling during ascent.

In the case of monodisperse droplets, r represents the average radius of the droplets. In Equation (2), neglecting higher-order terms in parameters A and B , the condensation rate (dq/dt) becomes proportional to the product of the mean radius (r) and supersaturation (S), expressed as:

$$\beta \frac{dq}{dt} \simeq \alpha(N) r S. \quad (3)$$

This proportionality is thus captured by the coefficient $\alpha(N)$, defined as:

$$\alpha(N) = 4\pi\rho_w\beta DNr. \quad (4)$$

Here, ρ_w is the water density, N is the number concentration of droplets (particles per unit volume), β is a constant related to latent heat release (see Appendix A), and D is a diffusion coefficient. The dependence of $\alpha(N)$ on particle concentration (N) is often omitted when N is not a key factor.

The term rS in Equation (3) resembles a predator-prey term. Larger particles and higher supersaturation values (rS) correspond to a higher rate of humidity consumption. Conversely, smaller particles and lower supersaturation lead to less humidity consumption.

Furthermore, $\alpha(N)$ is related to the phase-relaxation timescale (τ_p) through the relation $\tau_p = (r\alpha(N))^{-1}$. This timescale represents the time required for supersaturation to return to equilibrium (Korolev and Mazin, 2003; Prabhakaran et al., 2020).

The supersaturation-radius-Köhler (SRK) equations, with Eqns (2), (3), and (1) corresponding to each term, describe CCN activation within a cloud parcel that has external sources of supersaturation. In warm clouds, supersaturation typically remains below a few percent (Khain and Pinsky, 2018; Altaratz et al., 2021). Therefore, it is common practice to simplify Eq. (2) using the approximation $1 + S \approx 1$ (see, e.g., Khain and Pinsky (2018)). However, this simplification neglects the nonlinear behavior of supersaturation, which can become significant at higher values and is crucial

for understanding the distribution of supersaturation in turbulent clouds (Gutiérrez and Furtado, 2024). For the case of monodisperse cloud particles embedded in an adiabatic air volume, the SRK equations governing their growth rate can be expressed as:

$$\begin{cases} \dot{S} = \tau^{-1} - \alpha(N)rS & \text{(SRKa)} \\ \dot{r}^2 = 2D(S - f(r)), & \text{(SRKb)} \end{cases}$$

where S denotes supersaturation, and f , the Köhler curve.

2.1 Stability analysis for activation

In line with Köhler's equation (1), the activation/deactivation of a cloud droplet corresponds to the instability/stability of the variable r^2 of the SRK equation. We thus perform the linear stability analysis. Setting $\dot{S} = \dot{r}^2 = 0$, we find a unique equilibrium (S_0, r_0^2) , satisfying $r_0^2 > 0$:

$$S_0 = \frac{1}{\tau\alpha} \sqrt{\frac{A - \frac{1}{\tau\alpha}}{B}}, \quad (6a)$$

$$r_0^2 = \frac{B}{A - \frac{1}{\tau\alpha}}, \quad (6b)$$

where $(\tau\alpha)^{-1}$ has the units of length. The immediate observation is that the equilibrium (S_0, r_0^2) must lie on the Köhler curve in the S - r^2 -space, as shown in (SRKb). Moreover, the value of τ^{-1} , as the source term for S , determines the following:

- (i) If $\tau^{-1} = 0$, then $r_0^2 = r_c^2/3 = A/B$.
- (ii) If $\tau^{-1} < A\alpha$, (S_0, r_0^2) is an equilibrium.
- (iii) If $\tau^{-1} = 2A\alpha/3$, $r_0^2 = r_c^2$.
- (iv) As τ^{-1} approaches $A\alpha$, we have $\lim_{\tau^{-1} \rightarrow A\alpha^+} r_0^2 = \infty$.
- (v) If $\tau^{-1} > A\alpha$, there are no equilibria.
- (vi) If supersaturation is decreased, $\tau^{-1} < 0$, $S_0 < 0$ and $r_0^2 > 0$.

The presence of equilibria is determined by the interplay of the $(\tau\alpha)^{-1}$ -factor and the curvature coefficient, A , whereas the chemistry coefficient B only determines the location of the equilibrium.

The Jacobian matrix of the SRK equation determines the linear stability of the equilibrium (r_0^2, S_0) . A careful analysis of such matrix reveals the following results—the calculations are detailed in appendices B and B1—:

- (i) If $\tau^{-1} < 2A\alpha/3$, (r_0^2, S_0) is stable and therefore, CCN do not activate.
- (ii) If $\alpha < \frac{4A^3}{243B^2}D$, (r_0^2, S_0) is linearly unstable for some $2A\alpha/3 < \tau^{-1} < A\alpha$.

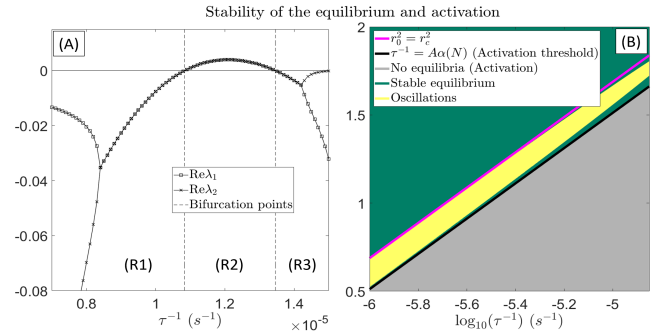


Figure 2. Panel (A): The squared and crossed lines show the real parts of the eigenvalues λ_1, λ_2 of the Jacobian of the SRK equation evaluated at the equilibrium (S_0, r_0^2) of Eq. (6) as a function for τ^{-1} , for $N = 50\text{cm}^{-3}$. The vertical dashed lines indicate where the equilibrium loses stability. **Panel (B):** The dark-green path corresponds to configurations in τ^{-1} and N where the SRK equation is linearly stable. At the gray area, the activation threshold is surpassed and the equilibrium Eq. (6) is not well defined. At the yellow area, the SRK system is linearly unstable and supports oscillations. The magenta and black lines satisfy $r_0^2 = r_c^2$ and $\tau^{-1} = A\alpha(N)$, respectively.

- (iii) If $\alpha > \frac{4A^3}{243B^2}D$ and $2A\alpha/3 < \tau^{-1} < A\alpha$, (r_0^2, S_0) is stable, although $r_0^2 > r_c^2$.

The proof of item (i) is found in Appendix B, and that of items (ii) and (iii) in Appendix B1.

It follows from the activation threshold $\alpha(N)A$, that the larger particle concentration N is, the more difficult it is to activate cloud droplets. Contrarily, if $\alpha(N) \approx 0$, a minimal updraft will make τ^{-1} positive and induce activation. In case of $f(r)$ not being present in Eq. (SRKb), the system does not admit equilibria. As can be observed by direct computation; see Devenish et al. (2016) for a more detailed analytical work.

3 Case study

We evaluate our analytical framework for an air parcel at a temperature and pressure of $T = 283\text{K}$ and $P = 10^5\text{Pa}$. We assume that the cloud is seeded with salt CCN with dry radii of $0.065\mu\text{m}$. This gives the curvature and chemistry coefficients of $A = 1.4 \cdot 10^{-3}\mu\text{m}$ and $B = 3.5 \cdot 10^{-4}\mu\text{m}^3$. Thus, the critical Köhler parameters are:

$$r_c^2 = 0.75\mu\text{m}^2, \quad (7a)$$

$$S_c = 0.108\%. \quad (7b)$$

The rest of model parameters are found in Table 1.

We now specify droplet number concentration, $N = 50\text{cm}^{-3}$ which gives $\alpha = 0.011(\mu\text{ms})^{-1}$, providing the activation threshold for $\tau^{-1} = A\alpha = 1.54 \cdot 10^{-5}\text{s}^{-1}$. The stability of the SRK system is determined by the largest real part

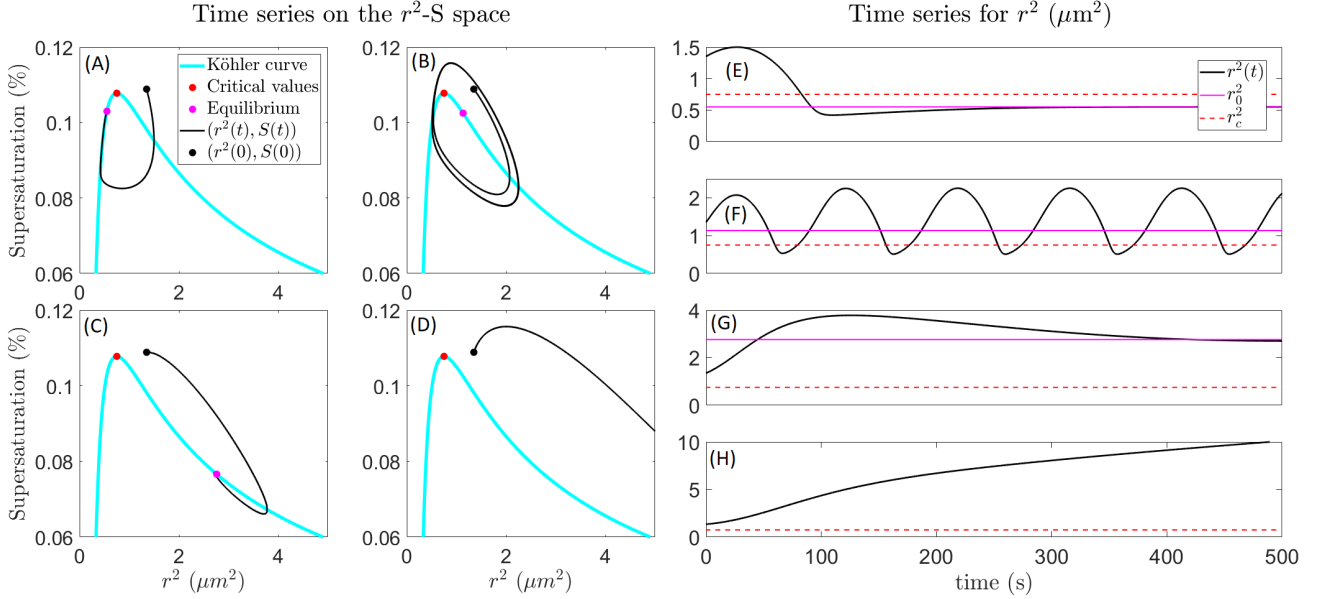


Figure 3. Panel (A): solution of the SRK equation in the r^2 -S space for the parameters in Table 1, $N = 50\text{cm}^{-3}$, $\tau^{-1} = 8.4 \cdot 10^{-4}\% \text{s}^{-1}$. This gives Jacobian eigenvalues $\lambda = -0.0352 \pm 0.0056i$. Panel (B): same as panel (A), for $\tau^{-1} = 1.2 \cdot 10^{-3}\% \text{s}^{-1}$ and $\lambda = 0.004 \pm 0.168i$. Panel (C): same as panel (A), for $\tau^{-1} = 1.4 \cdot 10^{-3}\% \text{s}^{-1}$ and $\lambda = 0.004 \pm 0.168i$. Panel (D): same as panel (A), for $\tau^{-1} = 1.8 \cdot 10^{-3}\% \text{s}^{-1}$, where the system has no equilibria. Panels (E), (F), (G) and (H): $r^2(t)$ against time, with the parameter configuration of Panels (A), (B), (C) and (D), respectively. Note that in panels (D) and (H) there are no magenta dot and line, respectively, since there are no equilibria in this case—see Eq. (6)—.

Table 1. Parameter configuration for the SRK equation. $T = 283\text{K}$ and $P = 10^5\text{Pa}$.

A [μm]	B [μm^3]	β [m^3kg^{-1}]	D [$\mu\text{m}^2\text{s}^{-1}$]
$1.4 \cdot 10^{-3}$	$3.5 \cdot 10^{-4}$	$3.5 \cdot 10^2$	50

of the eigenvalues λ_1, λ_2 of the linearized equation around (r_0^2, S_0) vs. τ^{-1} , here shown in Fig. 2 (A). The lines with squares and crosses correspond to the real parts of the eigenvalues, which merge when they become complex, i.e. $\lambda_1 = \bar{\lambda}_2$. The vertical dashed lines indicate the values of τ^{-1} where (r_0^2, S_0) loses stability and bifurcates. Thus, three distinct regimes are found and labeled as (R1), (R2) and (R3). At regime (R1), the system is stable and activation cannot occur. At (R2), the equilibrium (S_0, r_0^2) loses stability giving two alternatives: either the system activates leading to $r^2(t) \rightarrow \infty$ as $t \rightarrow \infty$, or the solutions of the SRK equation converge to a limit cycle (Guckenheimer and Holmes, 1983). Finally, at regime (R3), the SRK equation is stable, but converges to an equilibrium radius r_0 larger than Köhler's critical value r_c . To demonstrate these regimes, the SRK equations were numerically integrated and shown in the r^2 -S space in Fig. (3). Panel (A) shows the stable deactivated regime (R1), with $\tau^{-1} < 2A\alpha/3$. Panel (B) reveals that the linearly unstable regime (R2) with $\tau^{-1} < A\alpha$ is in fact a limit cycle, where

CCN activate and deactivate indefinitely. In panel (C), the system equilibrates at $r_0^2 > r_c^2$, i.e. regime (R3). And in panel (D), $\tau^{-1} > A\alpha$ so that CCN activate and, $r^2(t) \rightarrow \infty$. Panels (E), (F), (G) and (H) are the time series of the squared-radius $r^2(t)$ vs. time.

Changes in the particle concentration N affect the stability of (r_0^2, S_0) . In Fig. 2 (B) we plot the largest real part of the eigenvalues λ_1, λ_2 of J against τ^{-1} and N . Values in the gray triangle, below the black diagonal line lead to an activated family of CCN. Such line is computed from the activation threshold $\tau^{-1} = A\alpha$. The green area indicates configurations that lead to stable and inactive CCN populations. The magenta diagonal line satisfies $\tau^{-1} = 2A\alpha/3$, the values where $r_0^2 = r_c^2$. The yellow diagonal strip corresponds to linearly unstable (r_0^2, S_0) , which suggest the presence of oscillations as shown in panel (B) of Fig. 3.

Regarding the oscillatory behavior shown in Fig. 3(B), we demonstrate its dependence on $\alpha(N)$ in Fig. 4. First, we plot the equilibrium (r_0^2, S_0) against $\alpha(N)$, around which the limit cycle oscillates. Panels (B), (C) and (D) show the dependence of the limit cycle amplitude on N . The supersaturation rate τ^{-1} is taken as 5% above the bifurcation point where the SRK system at the equilibrium loses stability. As N grows, the cycle amplitude shrinks and, in fact, for $\alpha(N) > \frac{4A^3}{243B^2}D$, oscillations can no longer exist, as proved in Appendix B1. Also, the length of the interval of τ^{-1} sustaining oscillations

depends sensitively on the CCN dry radius as shown in Appendix A5.

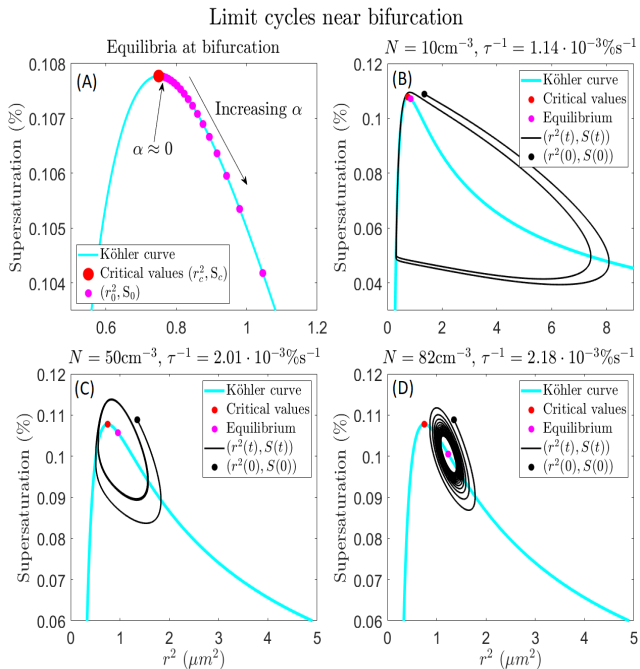


Figure 4. Equilibria and solutions of the SRK equation for the parameters of Table 1 and for N and τ^{-1} specified in the titles. **Panel (A):** Location of the equilibrium (r_0^2, S_0) as a function of $\alpha(N)$. **Panels (B), (C) and (D):** The black curve shows the solution of the SRK equation starting at the initial conditions shown in the black dot, the cyan line shows the Köhler curve, the red dot is the Köhler critical values (r_c^2, S_c) , and the magenta dot shows the equilibrium given by Eq. (6). The value of τ^{-1} is chosen 5% above the point where the equilibrium loses stability, i.e. the bifurcation point.

4 Concluding remarks

In this study, we approached the problem of droplet activation from a multi-particle perspective. We coupled the supersaturation budget to Köhler’s equation and explored the system’s behavior as a function of updrafts as the supersaturation source τ^{-1} and the droplet concentration N . Four main conclusions can be drawn from this theoretical analysis:

- (i) Only when the supersaturation timescale satisfies $\tau^{-1} > A\alpha$ do CCN activate. For instance, in the conditions of Section 3, a polluted cloud with concentration around 1000cm^{-3} and undergoing updrafts of less than 0.5ms^{-1} will not activate.
- (ii) Weak updrafts are not enough to attain activation: only when the supersaturation timescale satisfies $\tau^{-1} > A\alpha$ do CCN activate.

(ii) When $\tau^{-1} < 2A\alpha/3$, the SRK equations are linearly stable, and CCN do not activate, even if the initial sizes of humidified aerosols exceed Köhler’s critical radius r_c .

(iii) Droplet radii can stabilize around an equilibrium value r_0 greater than Köhler’s critical radius r_c . When $\tau^{-1} = 2A\alpha/3$, $r_0 = r_c$.

(iv) In a weakly lifted and sparsely populated air parcel, the SRK equation allows the existence of limit cycles, where CCN activates and deactivates indefinitely. As τ^{-1} is increased/decreased, the limit cycle appears/disappears, suggesting that the system undergoes a Hopf bifurcation (Guckenheimer and Holmes, 1983, Chapter 3).

Typically, haze growth is not accounted for in cloud models due to the high temporal resolution needed (Khain and Pinsky, 2018, §5.3), although there are models that determine wet aerosol growth during activation (Pinsky et al., 2008; Magaritz-Ronen et al., 2016). Generally, supersaturation is calculated at each grid point and timestep, and so if the critical radius r_c , according to which haze particles with a radius larger than r_c are deemed activated. The present analyses, however, show that seemingly active droplets— with a radius larger than r_c — can remain in equilibrium in weak updraft conditions that imply small supersaturation source, driven by the balance between condensation and supersaturation input, i.e., creating an intermediate regime in between haze and fully activated droplets. Such thermodynamic conditions are especially relevant to small, warm clouds that exhibit weak updrafts. It is then anticipated that turbulent fluctuations are critical under these conditions as they could trigger transitions between haze and activated droplets (Prabhakaran et al., 2020).

The extension of the analytical investigation of Köhler’s equation coupled to supersaturation should be done in two main directions. One concerns the effects of turbulent supersaturation fluctuations and their role in modifying activation thresholds, as is observed in general hysteretic processes (Berglund and Gentz, 2002). It is, then, expected that the addition of noise— coming from turbulent updrafts, for instance— will modify firstly, Köhler’s critical radius and supersaturation and, secondly, the stability of the SRK equation. A second direction should address lifting the monodisperse assumption and analyzing its effects on activation following the work of Pinsky et al. (2014), where the supersaturation budget and size distribution evolution are investigated. The addition of CCN with different dry radii or chemical compositions will translate into a substantial increase in the problem’s dimensionality, making it more difficult to extract analytical information. Suitable averaging, mean-field, or dimension-reduction techniques could help in this task.

Code availability. The used code is available upon request.

Data availability. No data was used or produced in this study.

Appendix A: Thermodynamic parameters and notations

There are key thermodynamic parameters employed throughout the paper. All of these parameters are also found in the literature (Rogers and Yau, 1989; Pruppacher and Klett, 2010; Khain and Pinsky, 2018). We provide the explicit expressions here:

$$\beta = \frac{1}{q_v} + \frac{L_w^2}{c_p R_v T^2} \quad (\text{A1})$$

where $q_v[-]$ is the water vapor mixing ration, $L_w[\text{Jk}^{-1}]$ is the latent heat of evaporation, $c_p[\text{Jkg}^{-1}\text{K}^{-1}]$ is the specific heat capacity of moist air at constant pressure, $R_v[\text{Jkg}^{-1}\text{K}^{-1}]$ is the specific gas constant for water vapor and $T[\text{K}]$ is the temperature.

The adiabatic parameter a_0 is defined as:

$$a_0 = \frac{g}{T} \left(\frac{L_w}{c_p R_v T} - \frac{1}{R_a} \right), \quad (\text{A2})$$

where $g[\text{ms}^{-2}]$ is the acceleration due to gravity and $R_a[\text{Jkg}^{-1}\text{K}^{-1}]$ is the specific gas constant of moist air.

The diffusional parameter is:

$$D = \left(\frac{\rho_w L_w^2}{k R_v T^2} + \frac{\rho_w R_v T}{E_w(T) D_{eff}} \right)^{-1}, \quad (\text{A3})$$

where $\rho_w[\text{kgm}^{-3}]$ is the density of liquid water, $k[\text{Jm}^{-1}\text{s}^{-1}\text{K}^{-1}]$ is the air heat conductivity, $E_w(T)[\text{Nm}^{-2}]$ is the saturation vapor pressure over liquid water and $D_{eff}[\text{m}^2\text{s}^{-1}]$ is the water vapor diffusion in air coefficient.

Regarding the Köhler parameters, these are:

$$A = \frac{2\sigma_w}{\rho_w R_v T}, \quad (\text{A4})$$

where $\sigma_w[\text{Nm}^{-1}]$ is the surface tension equal to the work needed to increase the surface by a unit of square. Raoult's coefficient is:

$$B = r_d^3 \frac{v_N \Phi_s \delta_s M_w \rho_N}{M_N \rho_w}, \quad (\text{A5})$$

where $r_d[\text{m}]$ is the dry radius of the aerosol, $v_N[-]$ is the total number of ions produced by salt, $\Phi_s[-]$ is the molecular osmotic coefficient of a deviation from perfect solutions, $\delta_s[-]$ is the soluble fraction of the aerosol, $M_w[\text{Da}]$ is the molecular mass of water, $M_N[\text{Da}]$ is the molecular mass of salt and $\rho_N[\text{kgm}^{-3}]$ is the density of salty aerosols.

Appendix B: Stability and deactivation interval

The linear stability is determined by the eigenvalues of the Jacobian of the SRK equation evaluated at the equilibria

(S_0, r_0^2) of Eq. (6), which reads as:

$$\begin{aligned} J(S_0, r_0^2) &= \begin{bmatrix} -\alpha r_0 & -\frac{\alpha}{2} S_0 r_0^{-1} \\ 2D & 3DBr_0^{-2.5} - DA r_0^{-3} \end{bmatrix} \\ &= \begin{bmatrix} -\alpha r_0 & -\frac{1}{2} \tau^{-1} r_0^{-2} \\ 2D & Dr_0^{-3} \left(\frac{3}{\tau\alpha} - 2A \right) \end{bmatrix} \end{aligned} \quad (\text{B1})$$

In the limit of $\tau^{-1} \rightarrow 0$, we have that $J(S_0, R_0)$ is lower-triangular with negative diagonal entries yielding the stability of the equilibrium. For $\tau^{-1} > 0$, it is challenging to find an analytical expression for the eigenvalues as a function of τ^{-1} , yet there is a non-empty interval for which stability holds. This is gathered in the following proposition:

Proposition 1. *Consider the SRK equation, and its Jacobian—Eq. (B1)—evaluated at the equilibrium (S_0, r_0^2) given in Eq. (6). Suppose that the coefficients α, D, B, A are positive. Then for all τ^{-1} in the interval $(-\infty, 2A\alpha/3]$, the equilibrium (S_0, r_0^2) is linearly stable.*

Proof. To prove the stability of (S_0, r_0^2) we have to examine the real parts of the eigenvalues λ_1 and λ_2 of the Jacobian matrix J given in (B1). The trace $\text{Tr}(J)$ and determinant $|J|$, provide the well-known analytic expressions

$$\lambda_1 = \frac{\text{Tr}(J) + \sqrt{\text{Tr}(J)^2 - 4|J|}}{2}, \quad (\text{B2a})$$

$$\lambda_2 = \frac{\text{Tr}(J) - \sqrt{\text{Tr}(J)^2 - 4|J|}}{2}. \quad (\text{B2b})$$

Simple calculations show that

$$\begin{aligned} |J| &= -\alpha D r_0^{-2} \left(\frac{3}{\tau\alpha} - 2A \right) + \tau^{-1} D r_0^{-2} \\ &= 2D r_0^{-2} (A\alpha - \tau^{-1}). \end{aligned} \quad (\text{B3})$$

ensuring positivity of $|J|$ if and only if $\tau^{-1} < A\alpha$. Thus, from Eq. (B2), the sign of the trace $\text{Tr}(J)$ will determine the stability in the interval $\tau^{-1} < A\alpha$ when $|J| \geq 0$. Indeed, if the discriminant $\text{Tr}(J)^2 - 4|J|$ is negative, its square-root is a pure-imaginary value and, thus, the stability of (S_0, r_0^2) is determined by the sign of $\text{Tr}(J)$. If the discriminant is positive, we have the following triangle inequality:

$$|\text{Tr}(J)| \geq \sqrt{\text{Tr}(J)^2 - 4|J|}, \quad (\text{B4})$$

and hence, the trace $\text{Tr}(J)$ decides the stability. To see this, if $\text{Tr}(J)$ is negative, λ_2 in Eq. (B2) will clearly remain negative, but also λ_1 by virtue of Eq. (B4). Conversely, if $\text{Tr}(J)$ is positive, λ_1 will remain so and that is enough to ensure instability.

The trace is written as:

$$\text{Tr}(J) = -\alpha r_0 + D\alpha^{-1} r_0^{-3} (3\tau^{-1} - 2A\alpha), \quad (\text{B5})$$

from where we deduce that for $\tau^{-1} < 2A\alpha/3$, the trace is negative and, hence, $2A\alpha/3$ is a lower bound to the smallest

real zero of $\text{Tr}(J)$. This together with the determinant being positive for $\tau^{-1} < A\alpha$, we conclude that the equilibrium (S_0, r_0^2) is stable for $\tau^{-1} < 2A\alpha/3$. \square

B1 Oscillatory regime

For the occurrence of limit cycles, it is necessary that the Jacobian eigenvalues develop an imaginary part, so that $\lambda_1 = \tilde{\lambda}_2$ (Guckenheimer and Holmes, 1983). The value of τ^{-1} at which this happens is given by the equation $\text{Tr}(J(S_0, r_0^2))^2 = 4|J(S_0, r_0^2)|$ which is equivalent to solving the following polynomial equation:

$$\begin{aligned} & -\alpha^2 B^4 + D^2 \alpha^{-2} (3\tau^{-1} - 2A\alpha)(A - \tau^{-1} \alpha^{-1})^4 \\ & - 2DB^2 (3\tau^{-1} - 2A\alpha)(A - \tau^{-1} \alpha^{-1})^2 \\ & - 8DB^2 (A\alpha - \tau^{-1})(A - \tau^{-1} \alpha^{-1})^2 = 0. \end{aligned} \quad (\text{B6})$$

The solutions of this equation in the variable τ^{-1} , would give the location of the intersection of the two branches in Fig. 2. When eigenvalues have negative real parts, their imaginary component correspond to the oscillations in a damped equilibrium. Positivity of the real part yields instability and, the possible appearance of limit cycles. Notice that when $B = 0$, a solution of Eq. (B6) is given by $\tau^{-1} = A\alpha$.

The range of values of $\tau^{-1} < A\alpha$ where the equilibrium (r_0^2, S_0) is unstable is susceptible of supporting a limit cycle, as illustrated in Fig. 3B. For that, it is necessary the trace of the Jacobian $\text{Tr}(J)$ is positive, as per Eq. (B2). The zeros of the trace $\text{Tr}(J)$ satisfy the following cubic polynomial equation in the indeterminate τ^{-1} :

$$\begin{aligned} P(\tau^{-1}) &= 3D\tau^{-3} - 8DA\alpha\tau^{-2} \\ &+ 7DA^2\alpha^2\tau^{-1} - B^2\alpha^4 - 2DA^3\alpha^3 = 0. \end{aligned} \quad (\text{B7})$$

The roots of this polynomial are given explicitly in Appendix D. However, an examination of the signs of the coefficients reveals—by Descartes' rule of signs—that P has either one or three positive roots. Conversely, the reverse-sign polynomial $P_-(\tau^{-1})$ reads as

$$\begin{aligned} P_-(\tau^{-1}) &= P(-\tau^{-1}) \\ &= -3D\tau^{-3} - 8DA\alpha\tau^{-2} \\ &\quad - 7DA^2\alpha^2\tau^{-1} - B^2\alpha^4 - 2DA^3\alpha^3. \end{aligned} \quad (\text{B8})$$

The lack of sign-change in the coefficients of $P_-(\tau^{-1})$ shows that $P(\tau^{-1})$ does not have zeros for negative values of τ^{-1} . As a consequence, it is possible that (S_0, r_0^2) loses its stability for some values of τ^{-1} prior to the activation threshold, namely in the range $2A\alpha/3 < \tau^{-1} < A\alpha$. It is challenging, however, to determine whether in that range droplets activate yielding that the solutions $r^2(t)$ diverge to infinity, or whether they converge to a limit cycle, see e.g. Guckenheimer and Holmes (1983). Below we provide a sufficient condition on $\alpha(N)$ for the existence of positive eigenvalues for the trace $\text{Tr}(J)$ for values of $\tau^{-1} < A\alpha$.

Proposition 2. *In the conditions of Proposition 1, if $\alpha < \alpha_{max} = 4A^3D/(243B^2)$, there exists an interval $(\tau_a^{-1}, \tau_b^{-1}) \subset (0, A\alpha)$ such that the trace of the Jacobian $\text{Tr}(J)$ is positive.*

Proof. Since $\text{Tr}(J)$ is a function of τ^{-1} , we shall define, for notational convenience, $T(\tau^{-1}) = \text{Tr}(J)$, for every τ^{-1} in $(0, A\alpha)$. Additionally, we note that T is a smooth function in the interval $(0, A\alpha)$ and so is the polynomial P .

Step 1. As also noted in Eq. (B7), the zeros of the trace $\text{Tr}(J)$ are equivalent to those of $P(\tau^{-1})$ in the variable τ^{-1} . This is to say that $P(\tau^{-1}) = 0$ if and only if $T(\tau^{-1}) = 0$. However, this is only valid in the interval $(0, A\alpha)$, since the following limit holds:

$$\lim_{\tau^{-1} \rightarrow A\alpha^-} T(\tau^{-1}) = -\infty. \quad (\text{B9})$$

Furthermore, we have that $T(\tau^{-1}) > 0$ if and only if $P(\tau^{-1}) > 0$ and $T(\tau^{-1}) < 0$ if and only if $P(\tau^{-1}) < 0$.

Step 2. The local maximum and local minimum of P are located at $\tau^{-1} = 7A\alpha/9$ and $A\alpha$, respectively. This is calculated from the derivative of $P(\tau^{-1})$:

$$P'(\tau^{-1}) = 9D\tau^{-2} - 16DA\alpha\tau^{-1} + 7DA^2\alpha^2 = 0. \quad (\text{B10})$$

From where we obtain the roots $\tau^{-1} = 7A\alpha/9$ and $A\alpha$. Since we are only interested in the interval $(0, A\alpha)$, we shall focus on the value $\tau^{-1} = 7A\alpha/9$. Because cubic term coefficient $3D$ is positive, it follows that $\tau^{-1} = 7A\alpha/9$ is a local maximum.

Step 3. We turn to examine the sign of $P(7A\alpha/9)$. A direct evaluation provides the following expression:

$$P\left(\frac{7A\alpha}{9}\right) = \frac{4}{243}DA^3\alpha^3 - B^2\alpha^4. \quad (\text{B11})$$

Equalizing to zero, gives that if $\alpha < \frac{4A^3}{243B^2}D$, $P(7A\alpha/9) > 0$. Hence, in such case, there exists $\varepsilon > 0$ such that $P(\tau^{-1}) > 0$ for every τ^{-1} in the interval $(7A\alpha/9 - \varepsilon, 7A\alpha/9 + \varepsilon)$.

It is now enough to define $\tau_a^{-1} = 7A\alpha/9 - \varepsilon$ and $\tau_b^{-1} = 7A\alpha/9 + \varepsilon$ to obtain the desired result. \square

Appendix C: Dependence of oscillatory interval on B

While Raoult's factor B , defined on Eq. (A5) of Appendix A, does not play a role in determining the activation threshold, it is key in the presence of positive eigenvalues of the linearized SRK equation, as per Proposition 2. It was there found a maximum value α_{max} such that for every $\alpha(N)$ lower than α_{max} , the equilibrium (S_0, r_0^2) in Eq. (6) loses stability for supersaturation rates τ^{-1} lower than the activation threshold $A\alpha(N)$. Such maximum value α_{max} is:

$$\alpha_{max} = \frac{4A^3}{243B^2}D. \quad (\text{C1})$$

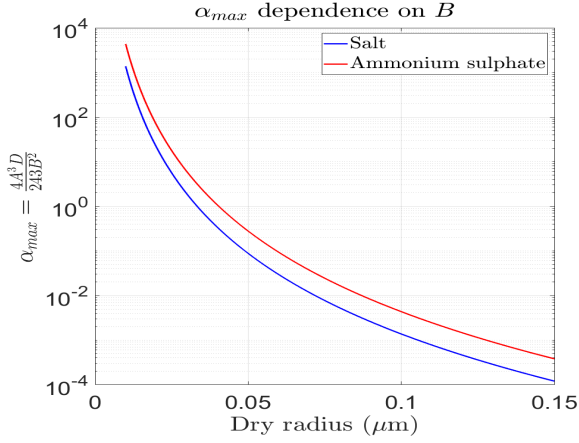


Figure C1. We plot $\alpha_{max} = \frac{4A^3}{243B^2}D$ as a function of aerosol dry radius and for two inorganic compounds indicated in the legend.

In Fig. C1 we plot the values of α_{max} as a function of aerosol dry radius, for salt (blue line) and ammonium sulfate (red line). We observe the sensitive dependence of α_{max} on dry radius. As a consequence of this, we can conclude that the interval of values of τ^{-1} that can lead to oscillatory behavior— analogous to that illustrated in Fig. 3(B)— increases with smaller dry aerosol radius.

Appendix D: Roots of the polynomial P in Eq. (B7)

The roots $\{x_1, x_2, x_3\}$ of the cubic polynomial $P(\cdot)$ with indeterminate τ^{-1} introduced in Eq. (B7) are given by:

$$x_1 = \sqrt[3]{\xi_1 + \sqrt{\xi_1^2 + \xi_2^3}} + \sqrt[3]{\xi_1 - \sqrt{\xi_1^2 + \xi_2^3}} + \frac{8A\alpha}{9}, \quad (D1)$$

$$x_2 = \left(-\frac{1}{2} + i\frac{\sqrt{3}}{2}\right) \sqrt[3]{\xi_1 + \sqrt{\xi_1^2 + \xi_2^3}} + \left(-\frac{1}{2} - i\frac{\sqrt{3}}{2}\right) \sqrt[3]{\xi_1 - \sqrt{\xi_1^2 + \xi_2^3}} + \frac{8A\alpha}{9}, \quad (D2)$$

$$x_3 = \left(-\frac{1}{2} - i\frac{\sqrt{3}}{2}\right) \sqrt[3]{\xi_1 + \sqrt{\xi_1^2 + \xi_2^3}} + \left(-\frac{1}{2} + i\frac{\sqrt{3}}{2}\right) \sqrt[3]{\xi_1 - \sqrt{\xi_1^2 + \xi_2^3}} + \frac{8A\alpha}{9}, \quad (D3)$$

where ξ_1 and ξ_2 are defined as:

$$\xi_1 = -\frac{1}{36}(A\alpha)^3 - \frac{B^2\alpha^4}{6D}, \quad (D4)$$

$$\xi_2 = -\frac{1}{34}(A\alpha)^2. \quad (D5)$$

If $\alpha < 4A^3D/(243B^2)$, the polynomial P has three real roots, as per Proposition 2. In this case, we assume that $x_1 \leq x_2 \leq x_3$. In particular, if $B = 0$, then $x_1 = 2A\alpha/3$, as observed by direct evaluation of $P(2A\alpha/3)$. Moreover, $x_2 = x_3 = A\alpha$ in this case. With this remark and the location of the local maximum of P at $7A\alpha/9$ obtained by solving Eq. (B10), we can estimate x_1 as the midpoint between $2A\alpha/3$ and $7A\alpha/9$:

$$x_1 \approx \frac{1}{2} \left(\frac{2}{3} + \frac{7}{9} \right) A\alpha = \frac{13}{18} A\alpha. \quad (D6)$$

Author contributions. MSG and MDC conceived the present idea. MSG lead the analyses, MDC and IK supported. MSG, MDC and IK discussed the results and wrote the manuscript. All authors critically contributed to the final form of the manuscript.

Competing interests. The authors declare no competing interests.

Acknowledgements. This work has been partially supported by the European Research Council (ERC) under the European Union's Horizon 2020 research and innovation program (grant agreement no. 810370). MSG is grateful to the Feinberg Graduate School for their support through the Dean of Faculty Fellowship.

References

- Altaratz, O., Koren, I., Agassi, E., Hirsch, E., Levi, Y., and Stav, N. (2021). The environmental conditions behind the formation of small (sub)cl clouds. *Geophysical research letters*, 48(23):e2021GL096242.
- Arabas, S. and Shima, S. (2017). On the ccn (de)activation nonlinearities. *Nonlinear Processes in Geophysics*, 24(3):535–542.
- Berglund, N. and Gentz, B. (2002). The effect of additive noise on dynamical hysteresis. *Nonlinearity*, 15(3):605.
- Devenish, B. J., Furtado, K., and Thomson, D. J. (2016). Analytical solutions of the supersaturation equation for a warm cloud. *Journal of the Atmospheric Sciences*, 73(9):3453–3465.
- Eytan, E., Koren, I., Altaratz, O., Kostinsky, A., and Ronen, A. (2020). Longwave radiative effect of the cloud twilight zone. *Nature Geoscience*, 13:669–673.
- Guckenheimer, J. and Holmes, P. (1983). *Nonlinear Oscillations, Dynamical Systems, and Bifurcations of Vector Fields*, volume 42. New-York Springer Verlag.
- Gutiérrez, M. S. and Furtado, K. (2024). Steady-state supersaturation distributions for clouds under turbulent forcing. *Journal of the Atmospheric Sciences*, 81(1):209–224.
- Hirsch, E., Koren, I., Altaratz, O., and Agassi, E. (2015). On the properties and radiative effects of small convective clouds during the eastern mediterranean summer. *Environmental Research Letters*, 10(4):044006.
- Hirsch, E., Koren, I., Altaratz, O., Levin, Z., and Agassi, E. (2017). Enhanced humidity pockets originating in the mid boundary layer as a mechanism of cloud formation below the lifting condensation level. *Environmental Research Letters*, 12(2):024020.

- Khain, A. P., BenMoshe, N., and Pokrovsky, A. (2008). Factors determining the impact of aerosols on surface precipitation from clouds: An attempt at classification. *Journal of the Atmospheric Sciences*, 65(6):1721 – 1748.
- Khain, A. P. and Pinsky, M. (2018). *Physical Processes in Clouds and Cloud Modeling*. Cambridge University Press.
- Köhler, H. (1936). The nucleus in and the growth of hygroscopic droplets. *Trans. Faraday Soc.*, 32:1152–1161.
- Koren, I., Remer, L. A., Kaufman, Y. J., Rudich, Y., and Martins, J. V. (2007). On the twilight zone between clouds and aerosols. *Geophysical research letters*, 34(8).
- Korolev, A. V. and Mazin, I. P. (2003). Supersaturation of water vapor in clouds. *J.Atmos.Sci.*, 60(24):2957–2974.
- Magaritz-Ronen, L., Pinsky, M., and Khain, A. (2016). Drizzle formation in stratocumulus clouds: effects of turbulent mixing. *Atmospheric Chemistry and Physics*, 16(3):1849–1862.
- Pinsky, M., Magaritz, L., Khain, A., Krasnov, O., and Sterkin, A. (2008). Investigation of droplet size distributions and drizzle formation using a new trajectory ensemble model. part i: Model description and first results in a nonmixing limit. *Journal of the Atmospheric Sciences*, 65(7):2064 – 2086.
- Pinsky, M., Mazin, I. P., Korolev, A., and Khain, A. (2013). Supersaturation and diffusional droplet growth in liquid clouds. *Journal of the Atmospheric Sciences*, 70(9):2778 – 2793.
- Pinsky, M., Mazin, I. P., Korolev, A., and Khain, A. (2014). Supersaturation and diffusional droplet growth in liquid clouds: Polydisperse spectra. *Journal of Geophysical Research: Atmospheres*, 119(22):12,872–12,887.
- Prabhakaran, P., Shawon, A. S. M., Kinney, G., Thomas, S., Cantrell, W., and Shaw, R. A. (2020). The role of turbulent fluctuations in aerosol activation and cloud formation. *Proceedings of the National Academy of Sciences*, 117(29):16831–16838.
- Pruppacher, H. R. and Klett, J. D. (2010). *Microphysics of Clouds and Precipitation*. Springer Dordrecht.
- Rogers, R. R. and Yau, M. (1989). *A Short Course in Cloud Physics*. Pergamon Press Oxford, New York, 3rd ed. edition.
- Squires, P. (1952). The growth of cloud drops by condensation. *Australian Journal of Chemistry*.
- Várnai, T. and Marshak, A. (2009). Modis observations of enhanced clear sky reflectance near clouds. *Geophysical Research Letters*, 36(6).
- Wallace, J. M. and Hobbs, P. V. (2006). *Atmospheric Science, an Introductory Survey*. Elsevier.
- Zelinka, M. D., Myers, T. A., McCoy, D. T., Po-Chedley, S., Caldwell, P. M., Ceppi, P., Klein, S. A., and Taylor, K. E. (2020). Causes of higher climate sensitivity in CMIP6 models. *Geophysical Research Letters*, 47(1):e2019GL085782.